JOURNAL OF GEOPHYSICAL RESEARCH, VOL. 112, B08411, doi:10.1029/2006JB004752, 2007

Modulation of the earthquake cycle at the southern San Andreas fault by lake loading

Karen Luttrell,[1] David Sandwell,[1] Bridget Smith-Konter,[1,2] Bruce Bills,[3,4] and Yehuda Bock[1]

Received 13 September 2006; revised 9 April 2007; accepted 14 May 2006; published 15 August 2007.

[1] Changes in the level of ancient Lake Cahuilla over the last 1500 years in the Salton Trough alter the state of stress by bending the lithosphere in response to the applied lake load and by varying the pore pressure magnitude within the crust. The recurrence interval of the lake is similar to the recurrence interval of rupture on the southern San Andreas and San Jacinto faults, both of which are partially covered by the lake at its highstand. Furthermore, four of the last five ruptures on the southern San Andreas fault have occurred near a time of substantial lake level change. We investigate the effect of Coulomb stress perturbations on local faults due to changing level of Lake Cahuilla to determine a possible role for the lake in affecting the timing of fault rupture. Coulomb stress is calculated with a three-dimensional model of an elastic plate overlying a viscoelastic half-space. Plate thickness and half-space relaxation time are adjusted to match observed vertical deformation since the last lake highstand. The lake cycle causes positive and negative Coulomb stress perturbations of 0.2–0.6 MPa on the southern San Andreas within the lake and 0.1–0.2 MPa on the southern San Andreas outside the lake. These Coulomb stress perturbations are comparable to stress magnitudes known to have triggered events at other faults along the North America-Pacific plate boundary.

Citation: Luttrell, K., D. Sandwell, B. Smith-Konter, B. Bills, and Y. Bock (2007), Modulation of the earthquake cycle at the southern San Andreas fault by lake loading, *J. Geophys. Res.*, *112*, B08411, doi:10.1029/2006JB004752.

1. Introduction

[2] The San Andreas fault system forms part of the boundary between the North American and Pacific plates, accommodating a total of about 40 mm/yr of right lateral slip [e.g., *Fay and Humphreys*, 2005]. The southern portion of the San Andreas fault system lies in the Salton Trough, a broad region of Southern California that includes the southern San Andreas fault (SAF), the southern San Jacinto fault (SJF), the Imperial fault (IF), and the Salton Sea. The Salton Trough is also a transitional tectonic regime between opening motion along a constructive plate margin in the Gulf of California and transform motion along the SAF system. This complex tectonic setting has the potential to produce large earthquakes, but the last 300 years have seen no major ruptures on the SAF and SJF and only one major earthquake on the IF [*Fialko*, 2006; *Fumal et al.*, 2002; *Gurrola and Rockwell*, 1996; *Shifflett et al.*, 2002; *Thomas and Rockwell*, 1996].

[3] The exact timing of a rupture on a fault is complicated and difficult to predict. However, the general readiness of a fault to fail can be characterized by the state of stress on that fault and changes to that stress, expressed through the Coulomb failure criteria [e.g., *King et al.*, 1994]. Nontectonic perturbations to the state of stress on a fault may also alter the Coulomb stress and thus the timing of the next event. In Japan, the changing vertical load of seasonally snow-covered mountains produces seasonal subsidence and seismicity [*Heki*, 2001; *Heki*, 2003]. On a much longer timescale, flexure of the lithosphere beneath the Fennoscandian ice sheet in the North Sea has been proposed as a mechanism to modulate stresses, affecting faulting style and seismicity [*Grollimund and Zoback*, 2000]. Another nontectonic source of stress perturbation, acting over intermediate timescales, is the vertical load caused by the filling and emptying of surface lakes.

[4] In this study we wish to investigate the feasibility of stress perturbations at the Salton Trough in response to ancient Lake Cahuilla influencing the timing of rupture on nearby faults. Numerous studies have used vertical surface deformation in response to lake loads to constrain subsurface rheology [e.g., *Bills et al.*, 2007, 1994; *Kaufmann and Amelung*, 2000], but few have examined their effect on faulting. Other studies have shown that induced seismicity may occur in response to reservoir level changes, either by direct response of elastic stress following loading or by delayed increase of pore pressure and decrease of effective

[1] Scripps Institution of Oceanography, La Jolla, California, USA.
[2] Now at Planetary Science and Life Detection Section, Jet Propulsion Laboratory, California Institute of Technology, Pasadena, California, USA.
[3] NASA Goddard Space Flight Center, Greenbelt, Maryland, USA.
[4] Also at Scripps Institution of Oceanography, La Jolla, California, USA.

0148-0227/07/2006JB004752$09.00

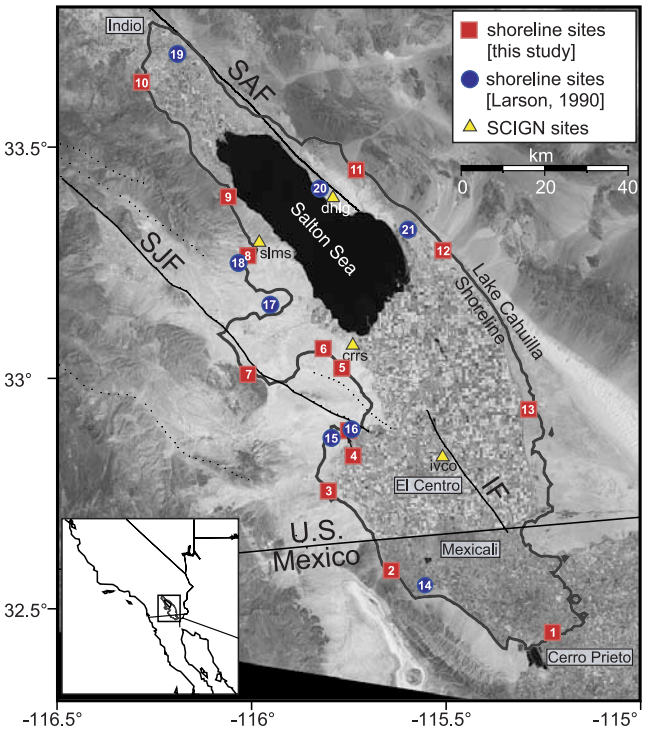

Figure 1. Ancient Lake Cahuilla region showing approximate location of the ancient shoreline (13 m above sea level), San Andreas fault (SAF), San Jacinto fault (SJF), and Imperial fault (IF). Other local faults not mentioned in the text are shown as dotted lines for reference. Sites of shoreline elevation surveys from this study are shown as red squares. Sites from *Larson* [1990] are shown as blue circles. Site numbers correspond to Table 1. Locations of SCIGN continuous GPS stations within ancient Lake Cahuilla are shown as yellow triangles (Table 2).

normal stress [e.g., *Simpson et al.*, 1988]. *Hetzel and Hampel* [2005] and *Hampel and Hetzel* [2006] examined lithospheric rebound in response to unloading in the Great Basin by the regression of Lake Bonneville and considered two mechanisms that affect the earthquake cycle. The direct removal of mass decreases vertical stress causing a decrease in slip rate on the normal Wasatch fault. Lithospheric rebound following the removal of mass alters horizontal stress promoting a faster slip rate. They found the combination of these mechanisms explains a Late Pleistocene increase in slip rate on the Wasatch and adjacent normal faults. Both the temporal and spatial scales of lake change we consider in this study are between those of reservoirs and Lake Bonneville. As such, we consider both the effects of three-dimensional (3-D) lithosphere deformation and of changes in pore pressure, but we consider only lithospheric rebound to be time-dependent.

1.1. Ancient Lake Cahuilla

[5] Ancient Lake Cahuilla is a freshwater lake (180 km × 50 km) that has periodically formed when the Colorado River drained north into the Salton Trough region of southern California instead of along its current course south through northern Mexico into the Sea of Cortez. At times of its highstands at 13 m above sea level [*Waters*, 1983], Lake Cahuilla extended from present-day Indio, California in the north to Cerro Prieto, Baja California Norte, Mexico in the south (Figure 1) covering parts of the southern SAF, SJF, and IF to a maximum depth of 90 m.

[6] The direction of flow of the Colorado River is controlled by the deposition of sediment at the river delta, which over time builds to form a natural dam. When enough sediment is deposited that the river is blocked from its southern course to the sea, flow turns northward into the Salton Trough and Lake Cahuilla forms quickly, filling in just 20 years to its maximum height of 13 m, controlled by the height of the sill at the southernmost edge [e.g., *Gurrola and Rockwell*, 1996; *Thomas and Rockwell*, 1996; *Waters*, 1983]. When in time the northern course becomes blocked by sediment, the Colorado resumes southern flow and the lake evaporates and becomes fully dry in approximately 60 years. The timing and duration of the last four lake highstands over the last 1300 years was studied by dating organic material from outcrop lake sediments and constraining these estimates to match the historical record (Figure 2) [*Gurrola and Rockwell*, 1996; *Sieh and Williams*, 1990; *Waters*, 1983]. *Waters* [1983] presents evidence for at least three clear highstands between the years AD 700 and 1500; furthermore *Gurrola and Rockwell* [1996] find three partial or total lakefall events between AD 1500 and 1700, represented in Figure 2 as a single falling event at the time the most recent lake began falling, between AD 1675 and 1687. While geologists do not yet agree on the timing and duration of even the most recent highstand, the changes in the volume of the lake are well constrained by the topography of the basin and the height of the sill. The most recent, though minor, change in lake level is the historically documented formation of the man-made Salton Sea in 1906, at a present-day elevation of 71 m below sea level [see *Oglesby*, 2005, and references therein].

1.2. Salton Trough Earthquakes

[7] The recurrence interval of the filling and draining of Lake Cahuilla is similar to the recurrence interval of major ruptures on the Southern SAF of 260 ± 100 years [*Shifflett et al.*, 2002] and documented activity on the SJF [*Gurrola and Rockwell*, 1996] (Figure 2). The occurrence of five ruptures on the southern SAF have been estimated between AD 1641–1711, 1450–1555, 1170–1290, 840–1150, and 770–890 with best averaged estimates of 1676, 1502, 1231, 982, and 825, respectively [*Fumal et al.*, 2002; *Sieh and Williams*, 1990]. The identification of these events at multiple sites along the SAF suggests that each of these was a major event rupturing at least the southernmost 200 km of the SAF. The last three ruptures on the southern SJF occurred between 1440 and 1637, 1280 and 1440–1640, and 820 and 1280 [*Gurrola and Rockwell*, 1996]. The most recent event is known to have occurred just before the ~1480–1660 inundation of Lake Cahuilla (T. Rockwell, personal communication, 2006) (see Figure 2). None of these events were historically recorded; all have been inferred from paleoseismology. The most recent major event on the IF was the historically recorded 1940 Imperial Valley earthquake (M_w = 7.0). Prior to that, an event has been identified late within the last highstand of Lake Cahuilla. No other major slip events are observed in the available

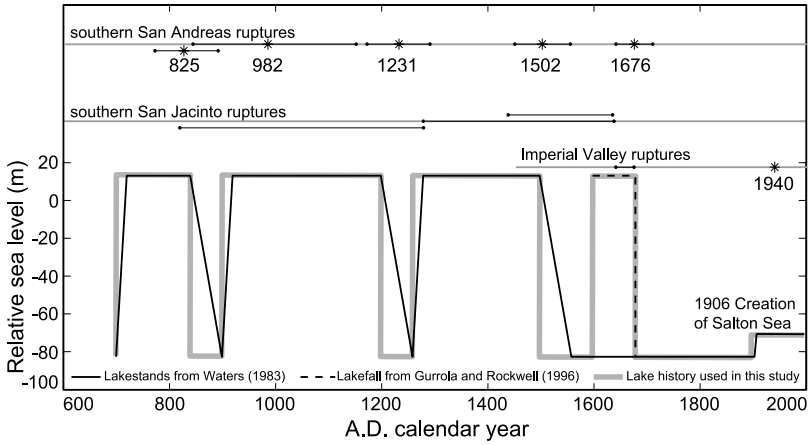

Figure 2. Lake level history from *Waters* [1983] (solid line) and *Gurrola and Rockwell* [1996] (dashed line), including the formation of the Salton Sea in 1906. The history used for models in this study is shown with a thick grey line. The last five southern SAF ruptures [*Fumal et al.*, 2002], last three southern SJF ruptures [*Gurrola and Rockwell*, 1996], and last two IF ruptures [*Thomas and Rockwell*, 1996] are also shown.

sediment record (since AD 1450) [*Thomas and Rockwell*, 1996].

[8] The similar recurrence intervals between lake level changes and major earthquakes could be mere coincidence. However, it is possible that there is a physical connection between the two phenomena. One possibility is that vertical motions associated with the major ruptures cause changes in the outflow direction of the Colorado River. In this case, the ruptures trigger the lake level changes. A second, more interesting possibility is that the change in stress due to the vertical load of the lake volume triggers the major events. It is the feasibility of this second possible connection that we explore in this study. If this model is correct, it could greatly impact our understanding of ruptures along the southern SAF system. In addition, one could calculate whether changing the configuration of the Salton Sea as proposed by the Salton Sea Authority (http://www.saltonsea.ca.gov/) would increase or decrease the probability of a major rupture on the southern SAF, which is believed to be late in the seismic cycle [*Fialko*, 2006].

2. Changes in Normal Stress Due to Lake Level Changes

[9] Slip on the upper locked portion (2–12 km) of a transform fault may be triggered by a reduction in fault stability, commonly characterized by a change in Coulomb stress [e.g., *King and Cocco*, 2001; *King et al.*, 1994; *Reasenberg and Simpson*, 1992],

$$\sigma_c = \sigma_s - \mu_f \sigma_n. \quad (1)$$

This includes both tectonic shear loading, in which deep slip gives rise to shear stress accumulation σ_s, and fault strength, equal to the coefficient of friction μ_f times the effective normal stress on the fault plane σ_n. We propose that changes in lake level modulate the earthquake cycle by changing the effective normal stress on major fault planes at seismogenic depth. We consider two types of perturbation to normal stress: those induced solely from the weight of the surface load, and those induced because the load is a fluid that interacts with a porous crust.

2.1. Lithosphere Bending Model

[10] Immediately after Lake Cahuilla fills, the Earth will respond to the weight of the surface load approximately as an elastic half-space. The spatial variations in the vertical load are defined by the lake depth, which is known from the topography of the Salton Trough. Convolving this load with the analytic flexure solution for the point response of an elastic half-space [*Love*, 1929] provides the exact displacement and stress. *Larson* [1990] calculated the displacement and stress due to changes in the level of Lake Cahuilla on an elastic half-space and found only small Coulomb stress changes at seismogenic depth (~10 kPa). Since this is 15 times smaller than shear stress associated with induced seismicity at other reservoirs, that study concluded that it is unlikely that this stress could trigger seismic activity. However, *Larson* [1990] also showed that the elastic half-space model provided a poor fit to the lake rebound data derived from present-day shoreline measurements. A thin elastic plate flexure model with an elastic thickness of about 40 km could better explain the shoreline rebound data.

[11] Figure 3a is a diagram of the lithosphere response to a vertical load considered in this study. A lake load having width comparable to the flexural wavelength of the elastic plate is applied. Initially, the Earth responds as an elastic half-space, but when the duration of the load exceeds the relaxation timescale of the asthenosphere, the plate bends. Consider a fault running parallel to the shoreline as shown in Figure 3a. At a seismogenic depth, for example 5 km, the downward flexing of the plate landward of the shoreline will cause extension (a decrease in normal stress), while the upward flexing of the plate within the lake will cause compression.

[12] We can calculate the magnitude of a Coulomb stress perturbation from a change in water level load by convolving the response of a unit point load on a thick elastic plate overlying a viscoelastic half-space with the true load distri-

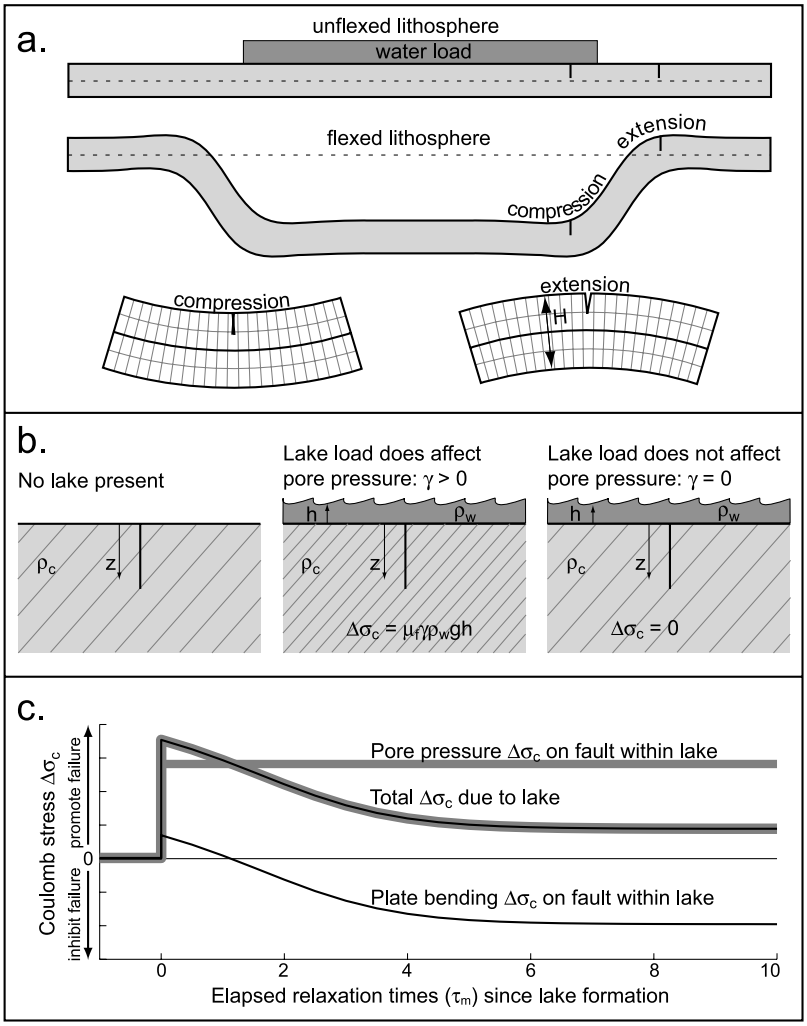

Figure 3. (a) Schematic representation of Coulomb stress variation by lithosphere flexure under a vertical load of lake water. Tick marks indicate faults inside and outside the lake boundary. In regions of compression, faults experience negative Coulomb stress perturbation, inhibiting failure. In regions of extension, faults experience positive Coulomb stress perturbation, promoting failure. (b) Schematic representation of Coulomb stress variation by change in pore pressure due to lake level change showing crust with pore pressure and no lake (left), crust with increased pore pressure in the presence of a lake (middle), and crust with unchanged pore pressure in the presence of a lake (right). An increase in lake level increases Coulomb stress, promoting failure. (c) Time evolution of Coulomb stress perturbation on a fault within the lake after a rise in lake level over 10 half-space relaxation times (τ_m). Pore pressure (thick grey line) responds instantaneously by increasing Coulomb stress. Plate flexure (dashed black line) has a small elastic response (instantaneous) increasing Coulomb stress, followed by a viscoelastic response (time dependent) decreasing Coulomb stress by a magnitude on the order of the increase caused by changes in pore pressure. The combined effects (thick grey and black line) are most important within the first five relaxation times after a change in lake level.

bution. We calculate the full 3-D problem semianalytically using a method developed by *Smith and Sandwell* [2003, 2004]. For both the plate and the half-space, we assume a Young's modulus of 70 GPa, a Poisson's ratio of 0.25, and a mantle material density of 3300 kg m^{-3}. The free parameters that we vary are elastic plate thickness H, half-space Maxwell relaxation time ($\tau_m = 2\eta/\mu$ where η and μ are the viscosity and shear modulus, respectively), and vertical load history. In the case of vertical loading by changing levels of water, the load $\rho_w g h(x, y)$ is known exactly in both spatial extent and magnitude because the topography is exactly known.

[13] We check the full 3-D model by considering a 2-D thin-elastic-plate approximation. The 3-D response should approximately match the thin elastic plate solution at infinite time and the elastic half-space solution at zero time. The vertical deflection $W(x)$ of a thin elastic plate of flexural rigidity D [N m] and flexural parameter α [m] in response to a step function vertical load of magnitude V_0 [N m^{-2}] is found by integrating the line-load solution [*Turcotte and*

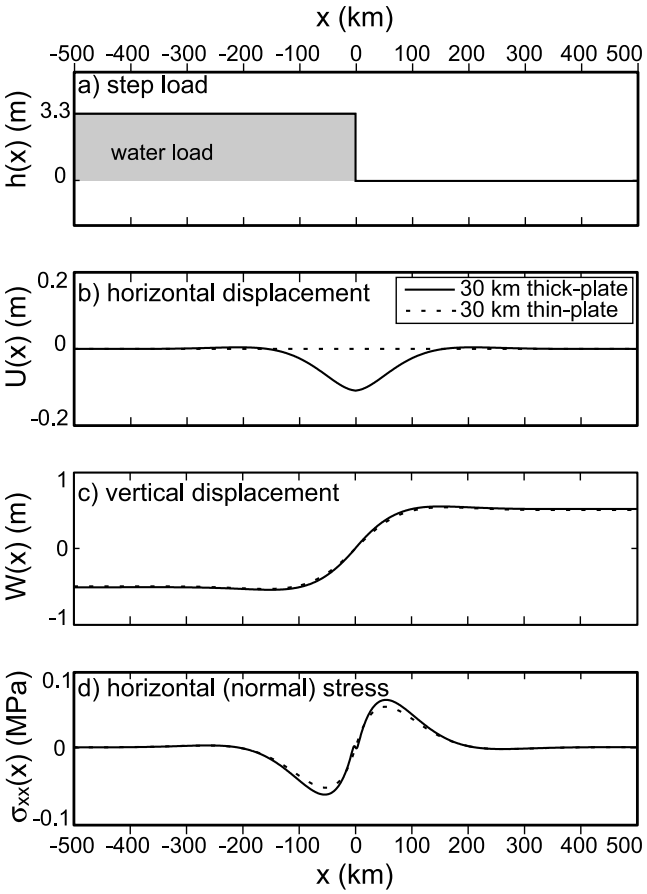

Figure 4. Displacement and stress of an elastic plate in response to a step water load. Solid line represents numerically calculated thick-plate flexure solution used throughout this study. Dashed line represents the analytic thin-plate flexure solution (equations (2) and (3)). Both solutions are calculated for a 30 km plate. Horizontal axis shows distance from edge of lake load. Vertical axis shows (a) applied water load, (b) horizontal surface displacement $U(x)$, (c) vertical surface displacement $W(x)$, and (d) horizontal (normal) stress $\sigma_{xx}(x)$ at seismogenic depth (5 km). The thin-plate flexure solution predicts no horizontal displacement. The thick-plate flexure solution shows an undulation in horizontal stress at the coastline due to local three-dimensional elastic stress effects.

Schubert, 2002, equation (3–130)] from the shoreline (x = 0) to infinite distance into the lake. The result is

$$W(x) = \frac{V_0 \alpha^4}{8D}\left(1 - e^{-|x|/\alpha}\cos\frac{|x|}{\alpha}\right)\text{sign}\,(x), \qquad (2)$$

where we have removed the mean deflection. The horizontal (normal) stress due to this load at a distance z_0 above the nodal plane is

$$\sigma_{xx} = \frac{3V_0\alpha^2}{H^2}\left(\frac{z_0}{H}\right)e^{-|x|/\alpha}\ \sin\left(\frac{|x|}{\alpha}\right)\text{sign}\,(x). \qquad (3)$$

[14] Figure 4 compares the analytical thin-plate flexure solution (dashed curves) for stress and displacement with the numerically calculated thick-plate flexure solution (solid curves). Figure 4a shows the applied step load of magnitude equivalent to 1 m of mantle density material, such that we expect a vertical displacement of 1 m beneath the load. Both the vertical deflection (Figure 4c) and the horizontal stress (Figure 4d) are antisymmetric about the edge of the step load at $x = 0$. The thick-plate solution shows almost exactly the same behavior as the thin-plate solution. There is a minor difference at the coastline where the thick-plate solution shows an undulation due to local 3-D elastic stress effects. There is one major difference between the two solutions; the thin-plate solution has no horizontal displacement $U(x)$ (Figure 4b), while the thick-plate solution has a net negative motion near the coastline. The good overall match between these solutions for vertical displacement and horizontal stress suggests that the thin-plate solution is adequate. However, the thick-plate solution also includes a viscoelastic response to accurately model the loading history. Moreover, it can accurately accommodate realistic coastlines. Computations of both solutions require the same amount of computer time.

[15] To provide a spatially accurate loading history, we use high-resolution (1 km) topography. Land elevations were derived from the Shuttle Radar Topography Mission data (http://www2.jpl.nasa.gov/srtm/) while elevations within the Salton Sea were derived by interpolating between digitized contours of bathymetry. The accurate topography accounts for the horizontal shifts in the coastline as lake level rises. Displacement and stress are computed at 1 km grid spacing and Coulomb stress is calculated on a vertical fault plane striking 45° West of North, the general trend of the SAF system.

2.2. Effect of Pore Pressure

[16] With the addition or removal of a load of water on the crust, the loading material interacts with the loaded material creating additional stresses. The presence of water in a fault may, for example, affect the coefficient of friction μ_f by altering fault minerals. In our analysis, we assume a constant coefficient of friction, $\mu_f = 0.6$ [*Byerlee*, 1978]. The lake load may also alter the stress on a fault by changing the effective normal stress, illustrated in Figure 3b. The effective horizontal normal stress σ_n on a fault is the difference between the inward pressure (primarily lithostatic) and the outward pore pressure due to the water-filled crust. If the lake level is increased by h and the water is free to percolate to seismogenic depth, then in time the pore pressure at that depth will increase by an amount $\Delta p = \rho_w g \Delta h$ to reach hydraulic equilibrium, where p is pore pressure, ρ_w is the water density (1000 kg m^{-3}), and g is the acceleration of gravity (9.8 m s^{-2}). This is equivalent to the "drained" pore pressure [e.g., *Roeloffs*, 1988a; *Roeloffs*, 1988b]. However, the system may not be able to reach equilibrium if, for example, the pore spaces in the crust are not fully connected to seismogenic depth. In this case, the change in normal stress due to lake rise is

$$\Delta\sigma_n = -\gamma\rho_w g h, \qquad (4)$$

Table 1a. Location and Elevation (Relative to GEOID03) of Lake Cahuilla Shoreline Sites Measured in This Study

Number in Figure 1	Location	Latitude	Longitude	Elevation ± Error, m
1	Cerro Prieto	32.448	−115.223	10.323 ± 0.299
2	Mexicali	32.582	−115.642	11.486 ± 0.387
3	Yuha Basin	32.753	−115.798	13.205 ± 0.083
4	Dry Wash	32.887	−115.745	12.862 ± 0.084
5	Superstition Hills	33.023	−115.766	11.773 ± 0.178
6	Elmore Ranch	33.063	−115.814	16.754 ± 0.391
7	Fish Creek Mountains	33.009	−116.006	12.079 ± 0.060
8	Salton City	33.266	−116.006	13.877 ± 0.379
9	Travertine Rock	33.391	−116.058	12.331 ± 0.146
10	La Quinta	33.637	−116.280	11.788 ± 0.056
11	Salt Creek Fan	33.452	−115.729	13.845 ± 0.047
12	Gas Line Road	33.277	−115.499	12.416 ± 0.086
13	Southeast Sand Bar	32.932	−115.285	11.841 ± 0.459

where $\gamma \in [0, 1]$ is a dimensionless parameter describing the ability of pore fluids to percolate at depth ($\gamma = 0$ for no fluid movement to depth, $\gamma = 1$ for hydrostatic pore pressure change at depth). The maximum magnitude of the direct Coulomb stress change is $\Delta\sigma_c = \mu_f \rho_w g h$. For the 90 m of lake level change associated with Lake Cahuilla and pore pressure fully able to penetrate to seismogenic depths ($\gamma = 1$), the increase in Coulomb stress will be 500 kPa.

[17] Though we use the equilibrated change in pore pressure, we assume that the time required for the crust to reach this equilibrium is much less than the timescale of lithospheric rebound. Thus we treat changes in pore pressure at depth as concurrent with lake level changes. This simplifies the problem to one relaxation time rather than two. Under this assumption, the predicted rate of change of Coulomb stress at a time of lake level change is an upper bound, as is the magnitude of Coulomb stress perturbation. Another simplifying assumption we make is to neglect lateral flow of pore fluids, such that beneath the lake, change in pore pressure is directly proportional to the change in water level directly above, and outside the lake there is no change in pore pressure. Including lateral flow would make the spatial pattern of predicted stress change more diffuse across lake shorelines.

2.3. Total Effect of Lake Change on Coulomb Stress

[18] Both the direct pore pressure and indirect plate bending effects should be considered when calculating the change in Coulomb stress induced by Lake Cahuilla. It is interesting to note that the spatial and temporal variations in stress at seismogenic depth will be rather complex functions. If the fault is beneath the lake, the pore pressure effect will cause a step increase in Coulomb stress, but this will decay to near zero after several viscoelastic relaxation times because of downward flexure of the plate (Figure 3c). A fault far from the lake that is not influenced by the direct hydrostatic effect will experience only the indirect effect of increasing Coulomb stress as the plate bends. A fault running between the high and low shorelines will experience a complicated time variation in stress because the shoreline changes position by up to 100 km as the lake fills. At seismogenic depth, Coulomb stress change due to plate bending is about equal in magnitude and opposite in sign to Coulomb stress change due to an increase in pore pressure.

3. Deformation and Rebound: Finding a Best-Fitting Model

[19] To constrain the model parameters of plate thickness (H) and relaxation time (τ_m), we measured the vertical rebound of the Lake Cahuilla area since the last lake fall by measuring the current elevation of observed ancient shoreline features (see Appendix A). The ancient shoreline elevation data collected from our survey are shown in Table 1a, along with data published by *Larson* [1990] (Table 1b). Data in Table 1a were collected with a GPS receiver measuring height above the reference ellipsoid (WGS84) and corrected to height above sea level with the GEOID03 model (http://www.ngs.noaa.gov/GEOID/GEOID03/). The ellipsoidal heights were estimated by 1 Hz instantaneous positioning [*Bock et al.*, 2000] of the field GPS receiver relative to the known geodetic coordinates of California Real Time Network (CRTN, http://sopac.ucsd.edu/projects/realtime/) sites. Data in Table 1b from *Larson* [1990] were collected by leveling to known benchmarks that denote height above sea level. We find that the

Table 1b. Location and Elevation of Lake Cahuilla Shoreline Sites From *Larson* [1990]

Number in Figure 1	Description	Latitude	Longitude	Elevation ± Error, m
14	A	32.55	−115.55	12.2 ± 0.1
15	C	32.87	−115.79	12.7 ± 0.1
16	F	32.89	−115.74	12.8 ± 0.1
17	D	33.16	−115.95	12.7 ± 0.1
18	G	33.25	−116.03	13.1 ± 0.1
19	B	33.70	−116.19	12.2 ± 0.1
20	H	33.41	−115.82	13.8 ± 0.1
21	E	33.32	−115.60	12.7 ± 0.1

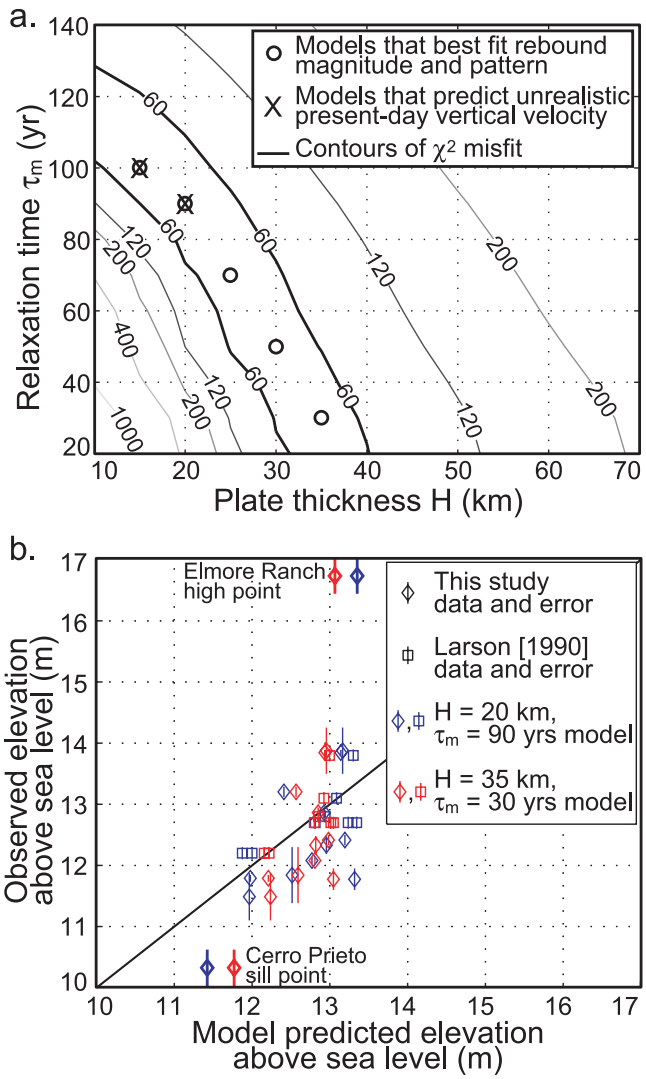

Figure 5. (a) Contours of χ^2 misfit for models with different (H, τ_m) values. Circles show (H, τ_m) pairs that fit the observed elevation data equally well. Crosses show (H, τ_m) pairs that predict vertical velocity today much higher than the observed velocity. (b) Predicted versus observed shoreline elevation at points given in Table 1. Observed elevation and error bars from this study (diamonds) and *Larson* [1990] (squares) is plotted on the vertical axis. Horizontal axis represents predicted elevation at each site calculated for two models with an equally low χ^2 value: a thinner plate (H = 20 km) with a more viscous half-space (τ_m = 90 years) (blue), and a thicker plate (H = 35 km) with a less viscous half-space (τ_m = 30 years) (red). Diagonal black line shows a perfect fit between observed and predicted elevation.

two approaches agree very well and that the largest uncertainty in the shoreline height measurement is related to identification of the shoreline marker (see Appendix A).

[20] We computed models of the vertical rebound due to lake loading for a plate thickness between 10 and 100 km and a half-space relaxation time between 20 years and 200 years (corresponding to half-space viscosity $\eta = \mu\tau_m/2$ of 10^{19}–10^{20} Pa s, given a shear modulus μ = 28 GPa). For each of these possible models, we compared the values of deformation expected at each of the 21 sites from Table 1 with the observed elevations above sea level. We can only detect the pattern and relative amplitude of the deformation; we cannot calculate the absolute elevation, thus our model has three free parameters: the plate thickness, the relaxation time, and an absolute vertical offset between the model-predicted and observed elevations.

[21] We computed the sum of squared residuals, where z_{mi} and z_{oi} are the modeled and observed elevations at each point, ε_i is the error of each observed measurement, and N is the total number of points (21),

$$\chi^2 = \frac{1}{N}\sum_{i=1}^{N}\frac{(z_{mi} - z_{oi})^2}{\varepsilon_i}, \tag{5}$$

and found no single best-fitting model (Figure 5a). Contours of misfit as a function of (H, τ_m) reveal a trade-off between plate thickness and relaxation time (i.e., half-space viscosity). A thinner plate can fit the data well with a more viscous half-space, while a thicker plate requires a less viscous half-space to fit the data equally well. Figure 5b shows the field-observed elevations from Tables 1a and 1b (diamonds and squares, respectively) along with their error bars plotted against the expected present-day model-predicted elevation for two equally best-fitting models, (H = 20 km, τ_m = 90 yr) and (H = 35 km, τ_m = 30 yr) (blue and red, respectively).

[22] It is possible to further constrain the model (H, τ_m) pairs by examining the vertical velocity that each predicts for today. For long relaxation times (thin plates), we expect that the Salton Trough would still be experiencing significant rebound from the last lake highstand; however, this constraint depends heavily on the timing of the last lake fall. We identified four continuous GPS receivers from the Southern California Integrated GPS Network (SCIGN) [*Hudnut et al.*, 2002] that are well within the bounds of Lake Cahuilla and would experience near-maximum uplift since the last lake fall (see Figure 1). Table 2a gives the locations and current vertical velocities of these sites (http://sopac.ucsd.edu/cgi-bin/refinedJavaTimeSeries.cgi). We also calculate the vertical velocity that each best-fitting (H, τ_m) model pair predicts today at each SCIGN site (Table 2b). The predominant vertical signal in this region is subsidence from the Salton Trough opening. Knowing the magnitude of Salton Trough subsidence, both expected from modeling (maximum −4 mm/yr, [*Smith and Sandwell*, 2003]) and observed from geodesy (∼−1 mm/yr, Table 2a), we determine that if the lake area were rebounding at anything more than a rate of 5 mm/yr, we would be able to observe the rebound at these four SCIGN sites. Hence all models that predict vertical uplift greater than 5 mm/yr at these points can be discounted (Figure 5a). This leaves us with two (H, τ_m) pairs to consider as model end members: (H = 25 km, τ_m = 70 yr) and (H = 35 km, τ_m = 30 yr). It is important to note that other nontectonic signals, for example a subsidence signal due to groundwater pumping for agriculture, could mask the rebound signal. However a groundwater signal would be more localized than the broad rebound deformation signal, so if such a signal had large enough amplitude to mask significant rebound, we would not expect

Table 2a. Location and Present-Day Vertical Velocity Observed at Four SCIGN Sites

SCIGN Site	dhlg	slms	crrs	ivco
Latitude	33.390	33.292	33.070	32.829
Longitude	−115.788	−115.978	−115.735	−115.507
Observed velocity, mm/yr	−1.7	−1.3	−1.8	−3.1

agreement at the four SCIGN sites. We are therefore confident that no significant lake rebound is occurring today in the Salton Trough.

[23] Around the lake, low rebound is expected at the far south and north and high rebound is expected in the east and west, closest to the deepest part of the lake (the current Salton Sea). The lowest point is the sill site at Cerro Prieto, shown in bold in Figure 5b. This is the single most important site because its elevation essentially sets the magnitude of the entire modeled rebound. It also has the second largest misfit, and no model we consider is able to fit both this point and the points closer to the present day Salton Sea. Our estimation of the sill elevation is consistent with other estimates [e.g., *Oglesby*, 2005], and the next lowest point at Mexicali (40 km northwest) is also lower than the models predict. It is possible that a geothermal plant near Cerro Prieto is causing local subsidence and making the measured sill height anomalously low. However the observation that both Cerro Prieto and Mexicali are low suggests a plate of uniform thickness may not be appropriate in the spreading region. The bulk of the data do not support the magnitude of rebound suggested by the sill point.

[24] The point with the worst misfit is the highest at Elmore Ranch. We do expect a large amount of rebound here because of its close proximity to the deepest part of the lake load, but there are other points at which equally high rebound is expected that have a much lower elevation and smaller misfit (e.g., Superstition Hills, Salton City, Larson points 17, 20, and 21). This leads us to believe that (1) the feature we measured at this point was not created by the most recent Lake Cahuilla highstand, (2) there are other tectonic sources of deformation at this location (e.g., interaction with an unmapped fault), or (3) we did measure the correct features but plate inhomogeneities (e.g., variable thickness, dike upwellings, cracks in the plate) are making this area rebound more than predicted. The effect of excluding the two furthest outlying points from our fit would be that the data would prefer a slightly thicker plate over a slightly more viscous half-space. The effect on the level of Coulomb stress perturbation on the SAF would be very small (e.g., 0.1 MPa difference).

4. Stress at Lake Cahuilla

[25] Before we consider fault stress perturbations due to real loading history, it is instructive to examine the response to a single lake cycle. Figure 6a shows the pattern of Coulomb stress for a vertical fault plane parallel to the SAF, due to the rise of the lake at time $t = 0\tau_m$ and the fall of the lake at $t = 10\tau_m$ for a plate thickness $H = 30$ km at 5 km depth. Figure 6b shows the Coulomb stress perturbation predicted at Bombay Beach, CA at the southern end of the SAF and within the boundaries of Lake Cahuilla, likely subject to pore pressure changes. Figure 6c shows Coulomb stress perturbation at Indio, CA, further north along the SAF and outside the shoreline of Lake Cahuilla, beyond the region affected by pore pressure variations. (Location of Bombay Beach (B) and Indio (I) is shown in the last frame of Figure 6a.) At $0\tau_m$, the pore pressure effect proportional to the depth of the lake is the dominant signal. By $2\tau_m$ much of the pore pressure effect has been negated by the bending of the lithosphere. The plate bending response is fully relaxed by $6\tau_m$. At $10\tau_m$, the lake load is removed and the Coulomb stress within the lake drops significantly; however, outside of the lake, the Coulomb stress increases slightly due to the elastic response of the lithosphere. By $16\tau_m$ the lithosphere is fully relaxed again. As part of our analysis, we considered the difference in stress between treating lake changes as instantaneous and treating them as gradual, as suggested by *Waters* [1983] (Figure 2). We found the difference in total Coulomb stress perturbation is small, but the difference in Coulomb stress rate is more significant. Fluid effects rather than rebound effects dominate the early stress behavior after a lake level change, so neglecting time-dependent lake level change affects stress in essentially the same way as neglecting time-dependent pore pressure response, a scenario previously discussed (see section 2.2).

[26] We calculate Coulomb stress perturbation due to the lake history shown in Figure 2, between A.D. 700 and 2000. Figure 7a shows Coulomb stress at Bombay Beach for a lithosphere with hydrostatic pore pressure ($\gamma = 1$) for end member models ($H = 25$ km, $\tau_m = 70$ yr, blue) and ($H = 35$ km, $\tau_m = 30$ yr, red). Over this period, perturbations of ±0.4–0.6 MPa are expected. Figure 7b shows Coulomb stress at Bombay Beach without the effect of pore pressure ($\gamma = 0$). The perturbations in Coulomb stress are, in general, smaller and less sudden. Figure 7c shows Coulomb stress at Indio, outside of the Lake Cahuilla shoreline and away from the effects of pore pressure. The perturbation magnitude is much smaller (0.2 MPa) due to increased distance from the deepest load.

[27] Figure 8a shows the regional difference in Coulomb stress from Lake Cahuilla (not including tectonic stress) between the most recent two southern SAF ruptures (1502 and 1676) calculated for ($H = 25$ km, $\tau_m = 70$ yr). During this time, the entire Lake Cahuilla region experiences an increase in modeled Coulomb stress. Coulomb stress at Bombay Beach on the SAF increases by 0.2–0.6 MPa depending on the effect of pore pressure. The SJF and IF

Table 2b. Present-Day Vertical Velocity Predicted at Four SCIGN Sites by Five Best-Fitting Model (H, τ_m) Pairs[a]

	Predicted Velocity at SCIGN Site, mm/yr			
Model (H, τ_m)	dhlg	slms	crrs	ivco
$H = 15$ km, $\tau_m = 100$ years[a]	15.6	14.8	16.2	10.8
$H = 20$ km, $\tau_m = 90$ years[a]	10.7	10.3	11.1	8.1
$H = 25$ km, $\tau_m = 70$ years[b]	5.2	5.1	5.4	4.2
$H = 30$ km, $\tau_m = 50$ years[b]	1.1	1.1	1.1	0.9
$H = 35$ km, $\tau_m = 30$ years[b]	0.02	0.02	0.02	0.02

[a]Models predicting uplift greater than 5 mm/yr (untenable).
[b]Models predicting uplift less than 5 mm/yr.

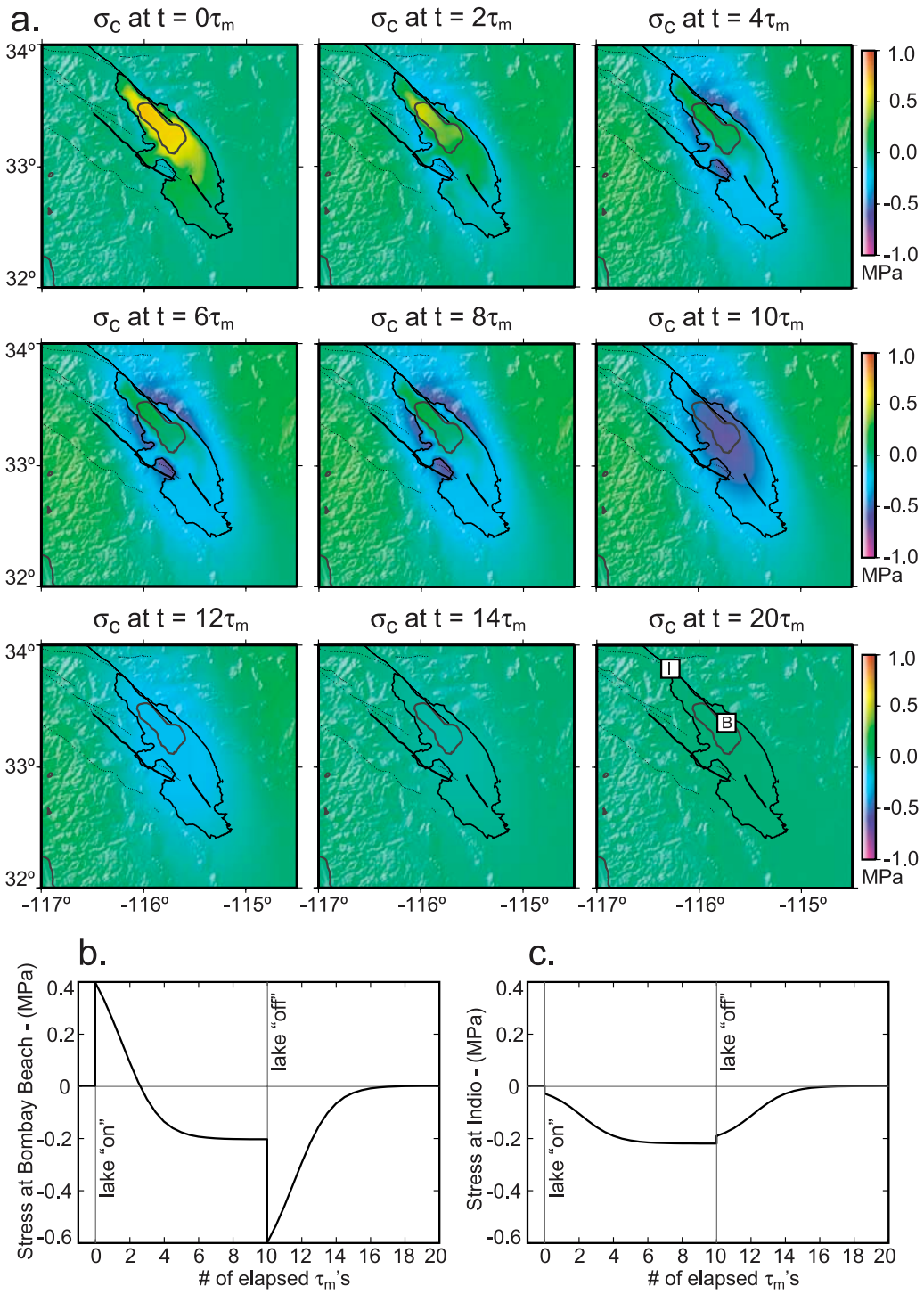

Figure 6. (a) Coulomb stress perturbations due to a single cycle of lake formation and desiccation. The lake fills at $0\tau_m$, remains full, and falls at $10\tau_m$. Negative Coulomb stress decreases the likeliness of rupture. Locations of Bombay Beach, CA (B) and Indio, CA (I) on the SAF are also shown. (b) Perturbation of Coulomb stress at Bombay Beach, within Lake Cahuilla. (c) Perturbation of Coulomb stress at Indio, outside of Lake Cahuilla.

experience smaller stress increases of 0.2–0.4 MPa. Figure 8b shows the stress perturbation since the last rupture. Within the lake, stress decreases due to the pore pressure effect. Around the lakeshore, particularly at the SJF, stress increases. Figures 8c and 8d show Coulomb stress perturbation between the last two ruptures and since the most recent rupture calculated for ($H = 35$ km, $\tau_m = 30$ years). The main differences between the two model predictions are

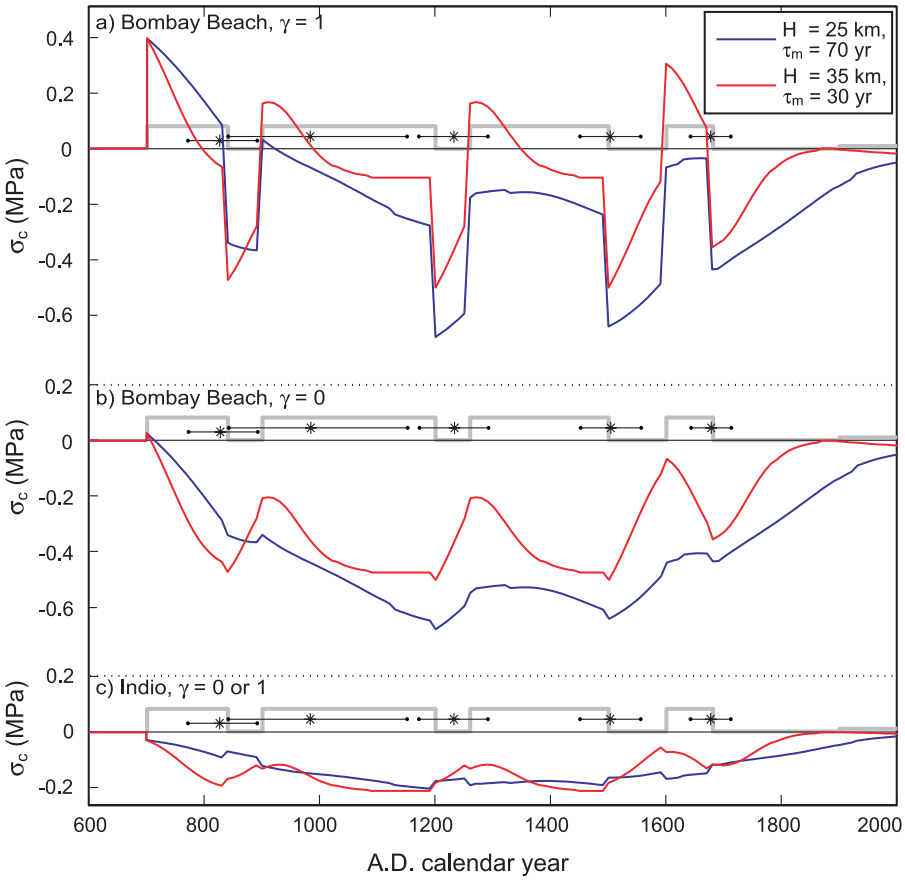

Figure 7. Coulomb stress perturbation from AD 700 to 2000 at (a) Bombay Beach within the lake with full pore pressure effect ($\gamma = 1$), (b) Bombay Beach with no pore pressure effect ($\gamma = 0$), and (c) and Indio outside of the lake with no pore pressure effect. Blue and red lines show stress from models with ($H = 25$ km, $\tau_m = 70$ years), and ($H = 35$ km, $\tau_m = 30$ years), respectively. Thick grey line shows timing of the lake level changes and black stars show timing and error of the last five Southern SAF ruptures (see Figure 2).

(1) the magnitudes tend to be higher for the shorter relaxation time, and (2) the plate deformation effect is broader for the thicker plate.

5. Discussion of Lake Cahuilla Stress Relevance

[28] The magnitude of Coulomb stress perturbation due to the changes in the level of Lake Cahuilla is, as expected, about 10 times smaller than tectonic loading that occurs between major earthquakes. It is, however, of comparable size to other effects that have been suggested to enact triggering. The postseismic deformation following the 1992 Landers earthquake, for example, led to Coulomb stress changes of 0.1–0.2 MPa in the vicinity of the 1999 Hector Mine earthquake, contributing to its failure [*Freed and Lin*, 2001]. Stress perturbation following lake level changes is certainly large enough to contribute to the stress budget on a given fault, but it is likely to only make an observable difference to faults that are critically stressed from tectonic loading (late in the seismic cycle).

[29] We would expect events to be triggered at times of increasing Coulomb stress following great tectonic loading (~1 recurrence interval since the last event). This could happen either: (1) shortly after lake level rise, due to an increase in pore pressure, or (2) in the time after a lake fall, due to fault-normal extension. Conversely, during times of low or falling Coulomb stress, we expect periods of quiescence. Four of the last five events are near times of lake level change; however, it is difficult to draw firm conclusions about a physical connection due to the large error bars in both lake history and timing of paleoevents.

[30] Better constraints are needed for both fault slip history and lake level history to determine if lake loading has been important in the real history of Salton Trough seismicity. For ruptures that occur near times of lake level change, knowing whether the rupture happened before, during, or after lake transition is key to understanding a possible causal relationship. In addition, knowing the date of a paleoevent (either seismic or lake related) to within one half-space relaxation time and understanding which lake falls were complete or partial will help refine the influence of lithospheric bending. We also expect that perturbations in Coulomb stress would trigger higher quantities of smaller events ($M < 5$) in addition to affecting the timing of very large events ($M > 7$). If the paleoactivity level were known with certainty, it would be an additional source of information to evaluate the lake loading effect.

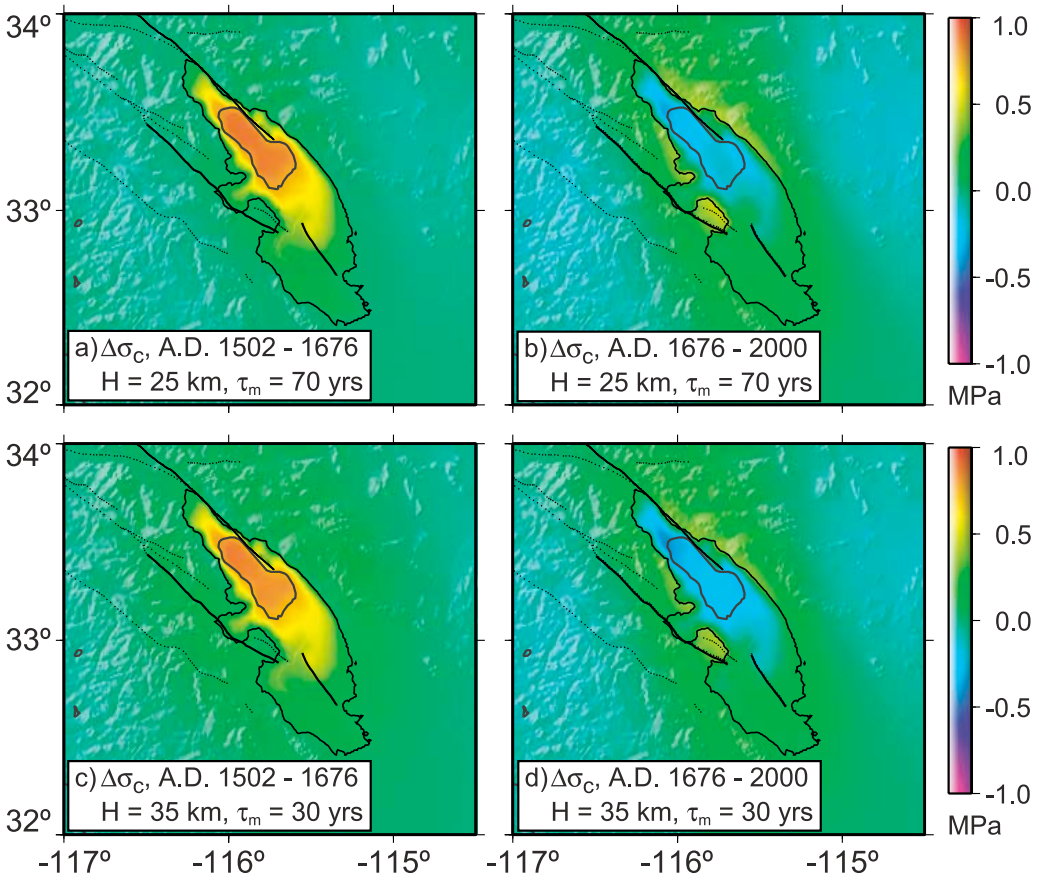

Figure 8. Coulomb stress perturbation in MPa (a and c) between the last two Southern SAF ruptures and (b and d) since the most recent rupture for two plausible model (H, τ_m) pairs: Figures 8a and 8b show H = 25 km, τ_m = 70 years, and Figures 8c and 8d show H = 35 km, τ_m = 30 years. Positive Coulomb stress perturbation promotes failure and negative inhibits failure.

[31] There has recently been much discussion in the literature about the need to reconcile fault slip rates interpreted from geologic measurements with those interpreted from geodetic ones [see *Bennett et al.*, 2004; *Matmon et al.*, 2005, and references therein]. There are two timescales that affect the earthquake cycle: the earthquake recurrence interval, which may be tens to thousands of years, and the Maxwell relaxation time, which may be tens to hundreds of years. Any perturbation of the earthquake cycle over longer geologic time periods requires another physical mechanism beyond those considered part of the earthquake cycle. It is over these longer timescales that fault slip rates along the San Andreas system seem to vary. Mechanisms that have been proposed to reconcile slip rate discrepancies include: transfer of slip rate between the SAF and the SJF [*Bennett et al.*, 2004], use of a more realistic rheology and rupture history [*Hetland and Hager*, 2006], higher geologic slip rate by finding more paleo-slip on faults [*Oskin et al.*, 2007], actual variations in slip rate caused by variations in fault strength and loading rate [*Chery and Vernant*, 2006], and actual variation in slip rate by changing normal stress in response to a vertical load [*Hampel and Hetzel*, 2006; *Hetzel and Hampel*, 2005]. The results of this study suggest that slip rate may in fact vary over timescales greater than or equal to the recurrence interval. Our hypothesis that lake loads modulate the earthquake cycle is a tenable explanation rooted in well-understood physics and could be extended to include other vertical loads on a broader spatial scale such as the differential load of rising sea level on a plate boundary.

[32] An interesting result of this analysis is the implications it suggests to the current Salton Sea. To control salinity and water elevation at the Salton Sea, a midlake dam has been proposed by the Salton Sea Authority to isolate the northern and southern portions of the lake, just north of Bombay Beach, which would involve some drawdown of lake level. Figure 9 shows the Coulomb stress perturbation today due to the 1906 formation of the Salton Sea, including the effect of pore pressure. The highest stresses of 0.1 MPa are within the lake itself. This model, with (H = 35 km, τ_m = 30 years), predicts only a slight decrease in Coulomb stress around the margins of the lake. While the stresses associated with the Salton Sea are smaller than those associated with ancient Lake Cahuilla, our analysis suggests the possible seismic impact of sudden changes in lake level should be considered in addition to the hazards of a dam nearby a major active fault.

[33] This analysis makes two simplifying assumptions about pore pressure resulting from lake level change. First, it assumes that pore fluids can move vertically but not

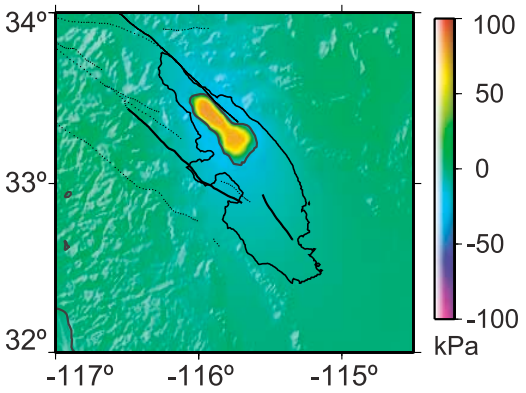

Figure 9. Coulomb stress response in kPa since formation of the Salton Sea in 1906. Maximum perturbation amplitude is ~90 kPa.

horizontally. Including horizontal flow would make the effect of pore pressure more diffuse, decreasing its influence within the lake and increasing its influence outside the lake boundary. Second, we assume that the changes in pore pressure occur instantaneously at all depths along a fault. Percolation of pore fluids is likely to be a time-dependent diffusive process. The error incurred by neglecting this time dependence will depend on its relation to the time dependence of lithospheric relaxation. If the fluid-flow relaxation time is much shorter than subsurface relaxation time from this load, then instantaneous fluid flow is a reasonable simplification. If the fluid-flow timescale is comparable to or longer than that of subsurface relaxation, then their combined Coulomb stress perturbation magnitude may be smaller by up to an order of magnitude.

[34] Modeling lithospheric bending with an elastic plate over a viscoelastic half-space is certainly a simplification of real subsurface rheology. This model does not include variations in viscosity as the geotherm increases with depth or variations in plate thickness expected in a complex tectonic region. Investigations at Lake Bonneville [*Bills et al.*, 1994] and Lake Lahontan [*Bills et al.*, 2007], 900 km to the northeast, inverted rebound data for viscosity and layer thickness of 7–10 layers and observed distinct upper crust, lower crust, and upper mantle viscosities (10^{24} Pa s, 10^{18-19} Pa s, and 10^{20-18} Pa s respectively). However the rebound signal at those lakes is 10s of m, more than an order of magnitude larger than the signal at Lake Cahuilla where rebound data are best fit by a 25–35 km plate over a halfspace of viscosity 10^{19} Pa s. Investigations of deformation following the 1938 filling of Lake Meade, 300 km to the north-northeast, found the 0.2 m pattern of subsidence could be fit equally well by a two-layer model (30 km elastic crust over viscoelastic half-space with viscosity 10^{18} Pa s) and a three-layer model (10 km elastic upper crust and a 20 km viscoelastic lower crust with viscosity $>10^{20}$ Pa s over a viscoelastic half-space with viscosity 10^{18} Pa s) [*Kaufmann and Amelung*, 2000]. Increasing model complexity to include 10 viscoelastic layers minimally affected the fit to rebound data. The results of these studies suggest that while Lake Cahuilla rebound data are likely insufficient for detailed analysis of subsurface rheology, they are satisfactory for estimating first-order rheologic parameters for the purpose of calculating bending stresses.

6. Conclusion

[35] We have explored the possibility of stress changes due to changes in pore pressure and isostatic rebound in response to the transient existence of Lake Cahuilla affecting the earthquake cycle on nearby faults by hastening or delaying rupture. Over the last 1300 years of lake rise and fall, Coulomb stress on the southern SAF has been perturbed 0.2–0.6 MPa within the lake and 0.1–0.2 MPa outside the lake. This stress perturbation is an order of magnitude smaller than Coulomb stress associated with tectonic loading. Therefore lake perturbations are likely to modulate the earthquake cycle only when faults are near critically stressed. Though the similarity in recurrence interval for the southern SAF and the filling/falling of Lake Cahuilla is intriguing and the lake-related mechanisms of stress perturbation are nontrivial, firm conclusions cannot be made without better constraints on the paleo history for the Salton Trough region.

Appendix A

A1. Geological Field Studies

[36] The following are descriptions of the field studies carried out between January 2006 and January 2007 around the ancient Lake Cahuilla shoreline. Sites were identified and features measured using a variety of techniques, each described here along with their respective sources and magnitudes of error.

[37] We made extensive use of a dual-frequency GPS receiver (Ashtech Z-12) sampling at 1 Hz to estimate precise ellipsoid heights of a number of site locations relative to the known geodetic coordinates of California Real Time Network (CRTN) sites, where coverage was available (http://sopac.ucsd.edu/projects/realtime/). In other locations we set up temporary 1 Hz base stations. Using the Geodetics RTD software in post-processing mode, we estimated receiver coordinates by instantaneous positioning, as described by *Bock et al.* [2000], of about 15–60 min of 1 Hz data collected at each field site. In this approach, each epoch of 1 Hz GPS observations of field receiver and CRTN site(s) are analyzed independently to estimate a series of 3-D geodetic coordinates, which are then averaged using robust statistics. Ellipsoid heights are converted to elevations (geoid/orthometric heights) using the GEOID03 model [http://www.ngs.noaa.gov/GEOID/GEOID03/].

A1.1. Surveys of Tufa-Covered Cliffs

[38] Along the western side of Lake Cahuilla there are several locations where the lake was bounded by high cliffs at the edge of the Fish Creek and Santa Rosa Mountains. During lake highstand, tufa deposits (layers of $CaCO_3$ deposited in warm freshwater in the presence of blue-green algae [e.g., *Nelson et al.*, 2005; *Oglesby*, 2005]) form along the cliffs at and below the waterline. These watermarks exist today and are easily recognized as the line between the dark outer deposit growth and the bare rock underneath. We measured this at three sites (Fish Creek Mountains, Travertine Rock, and La Quinta). In some sections, there were two tufa substances on the rocks: (1) an older, more friable beige

layer that covered the rocks to a higher level, and (2) a more recent sturdy black layer that covered the beige layer up to a height of a few feet below the height of the beige layer. The beige layer may represent a previous highstand at a different level or perhaps deposits from early in the lake highstand from before it subsided. For this study, we measured the height of the sturdy black layer of tufa. Though regionally the tufa line is quite flat, at close range there is some variation in its height depending on, for example, erosion since deposition, degree of shelter, and local wave energy. Since we were looking for the highest stand of the lake, we measured the height of the highest tufa within each 10-foot section.

[39] The heights were determined by using a leveling scope to sight to a particular feature to determine its height above the nearby GPS receiver. The processed GPS height is relative to the WGS84 reference ellipsoid and has an error of less than 5 mm. At each point, the height of the feature relative to the receiver was added to the GPS height above WGS84 and the GEOID03 correction to determine feature height above sea level. For each site, a single elevation was determined as the median of the local maximum measurements and the error is half the interquartile range.

A1.2. Survey at Gas Line Road

[40] Aerial photos of the Gas Line Road site show distinct color changes parallel to the expected shoreline location reoccurring periodically westward (toward the Salton Sea). We surveyed the highest (most eastward) color change visible in the aerial photos and found a mostly flat region with small (1–2 m) hills. We observed a regional delineation in the appearance of surface rocks, parallel to the 13-m National Elevation Data Set (NED) contour (approximate expected location of the Lake Cahuilla shoreline). Toward the Salton Sea, surface rocks were well-rounded, grey in color, and had a typical size of a few inches. Away from the Salton Sea, surface rocks were jagged, pink in color, and of the same typical size. We interpreted the well-rounded rocks as having spent much more time in water compared to the jagged rocks, and we interpreted the transition point between rounded and jagged rocks as the highest point where Lake Cahuilla waters were able to round the stones existing on its shore. A few hundred meters to the north, the color change visible in aerial photos no longer marks a transition between two types of rocks. Rather, it marks a transition between well-rounded, grey-colored pebbles and hard-packed sand with no pebbles on the surface. We measured the height of these features by taking GPS measurements at three locations along a 700 m stretch of shoreline and using a leveling scope to sight horizontally from the GPS stations to 10 other points exactly on the edge of the shoreline feature.

A1.3. Stationary Surveys of Constructional Berms

[41] Constructional sand berms are formed around lake edges by deposition of sediment carried by currents within a lake [e.g., *Adams et al.*, 1999; *Currey*, 1982]. Their crest is at or near the elevation of the lake. At four sites (Mexicali, Dry Wash, Elmore Ranch, and Salt Creek Fan) we identified the sand berms at the shoreline from their lighter color in aerial photography and LANDSAT images. In the field, we measured the elevation of the berm crest, away from vehicle tracks and other human demolition of the feature. The actual survey was conducted in the same manner as the Gas Line Road survey, sighting from a feature to a stationary GPS receiver with a leveling scope. Post analysis, we found the error involved with knowing the elevation of the berm crest is tolerably small (<0.1 m). The biggest problem with these sites is constraining the relationship between berm crest elevation today and water level at the time of lake highstand (see below).

A1.4. Mobile Surveys of Constructional Berms

[42] At four sites (Yuha Basin, Superstition Hills, Salton City, and Southeast Sandbar) sand berms were identified in the same manner as the stationary survey sites (see above) but were measured in a different way. In an attempt to expedite the survey, we mounted a GPS receiver sampling at 1 Hz on a low stable rolling platform that could be pulled by hand along and across the crest of a berm, ideally yielding many more data points, all at the desired elevation over a much shorter time. Postanalysis, however, we found that in a linear mobile survey, the desired elevation signal is somewhat masked by coexistent and unrelated dips and bumps in topography which would be easily avoided in a static survey. Thus the potential advantage of more data was nullified by the noise in that data, leading to larger errors (0.1–0.5 m) in elevation measurements at these sites. As with the stationary berm surveys, this error does not include the difficulty in constraining the relationship between berm crest elevation today and water level at the time of lake highstand (see below).

A1.5. Cerro Prieto

[43] The sill point at the southern end of Lake Cahuilla is the single most important point for establishing the magnitude of vertical rebound. To establish its location and elevation, we first examined contours of Shuttle Radar Topography Mission (SRTM) and National Elevation Data Set (NED) topography. While the NED 13-m contour closes south of Mexicali, Mexico, the SRTM 13-m contour is open between Lake Cahuilla and the Sea of Cortez. According to SRTM topography (3-min resolution), Lake Cahuilla is only isolated from the Sea of Cortez at elevations at or below 10.0 ± 0.299 m by a narrow 2 km wide strip of land east of Cerro Prieto volcano. NED likely has considerable errors outside of the U. S., so we used remotely derived SRTM for our analysis. However, the SRTM may have broad errors in elevation.

[44] We verified the accuracy of the SRTM elevations by comparing it with both Geoscience Laser Altimeter System (GLAS) tracks (vertical resolution <2 cm [*Fricker et al.*, 2005]) crossing the sill and GPS tracks taken from a receiver mounted to the roof of a vehicle driving across the sill region (this study). On the basis of these comparisons, we determined SRTM elevation requires a uniform offset correction of 0.323 m in the vicinity of the sill.

A2. Suggestion for Improvement of Data

[45] With improved accuracy and abundance of rebound measurements, we could acquire a more complete picture of the spatial extent and magnitude of Coulomb stress perturbations on faults in the study region. Currently, our least reliable data are those at sand berm sites. One way to improve our understanding of these sites would be to have LIDAR coverage with which to conduct a statistical analysis of the height, width, and extent of the berms. We were able to explore this potential method at Durmid Hill, a

region of tectonic uplift on the SAF east of the Salton Sea. During Lake Cahuilla highstands, portions of it stood above the water level as an island, and it was covered by the B4 Airborne Laser Swath Mapping (ALSM) topography survey, flown along the SAF and SJF with 0.5-m footprint resolution and 0.1 m height accuracy [*Bevis et al.*, 2005]. In these data and in the field, we observe concentric recessional terraces spreading out from the hill. In a histogram of the relevant section of topographic data, we were able to identify these terraces as distinct peaks because of the extra land at these elevations. If we had similar data around the Lake Cahuilla shoreline at each local setting, we could use statistical analyses to better understand the diffusive processes involved in berm profile evolution.

[46] In contrast to sand berm sites, tufa sites are much easier to identify and measure with small error for several reasons: (1) unlike berms and sorted surface rocks, tufa deposits change very little over 300 years, (2) tufa deposits extend along the entire length of the host cliff allowing for maximum redundancy in sampling, and (3) tufa deposits have little local variation in elevation. However, the greatest limitation in our shoreline elevation survey is the unknown relationship between the current elevation of a measured feature and the water elevation at the time of lake highstand. In the case of sand berms, this error is caused by erosion and diffusion so that the height of the feature today is likely not the same as it was at the time of the lake highstand. In the case of tufa deposits, this error is caused by the fact that the high line of tufa may form slightly higher or lower than the actual water level. We expect errors of this sort to be, at most, a few meters and count them as the most significant source of noise in our data.

[47] **Acknowledgments.** We thank Steven Micklethwaite and an anonymous reviewer for their help in improving the manuscript. We also thank Yuri Fialko and Donna Blackman for providing careful in-house reviews. We are grateful to Daniel Brothers, Joseph Becker, and Afton Van Zandt, who assisted in the fieldwork for this project. This research was supported by the National Science Foundation (OCE-0326707) and the Academic Senate of the University of California.

References

Adams, K. D., S. G. Wesnousky, and B. G. Bills (1999), Isostatic rebound, active faulting, and potential geomorphic effects in the Lake Lahontan basin, Nevada and California, *Geol. Soc. Am. Bull.*, *111*(12), 1739–1756.

Bennett, R. A., A. M. Friedrich, and K. P. Furlong (2004), Codependent histories of the San Andreas and San Jacinto fault zones from inversion of fault displacement rates, *Geology*, *32*(11), 961–964.

Bevis, M., et al. (2005), The B4 project: Scanning the San Andreas and San Jacinto fault zones, *Eos Trans. AGU*, *86*(52), Fall Meet. Suppl., Abstract H34B-01.

Bills, B. G., D. R. Currey, and G. A. Marshall (1994), Viscosity estimates for the crust and upper mantle from patterns of Lacustrine shoreline deformation in the eastern Great Basin, *J. Geophys. Res.*, *99*(B11), 22,059–22,086.

Bills, B., K. D. Adams, and S. G. Wesnousky (2007), Viscosity structure of the crust and upper mantle in western Nevada from isostatic rebound patterns of the Late Pleistocene Lake Lahontan high shoreline, *J. Geophys. Res.*, *112*, B06405, doi:10.1029/2005JB003941.

Bock, Y., R. M. Nikolaidis, P. J. de Jonge, and M. Bevis (2000), Instantaneous geodetic positioning at medium distances with the Global Positioning System, *J. Geophys. Res.*, *105*(B12), 28,223–28,253.

Byerlee, J. (1978), Friction of rocks, *Pure Appl. Geophys.*, *116*(4–5), 615–626.

Chery, J., and P. Vernant (2006), Lithospheric elasticity promotes episodic fault activity, *Earth Planet. Sci. Lett.*, *243*(1–2), 211–217.

Currey, D. R. (1982), Lake Bonneville: Selected features of relevance to neotectonic analysis, *U. S. Geol. Surv. Open File Rep.*, *82-1070*, 31 pp.

Fay, N. P., and E. D. Humphreys (2005), Fault slip rates, effects of elastic heterogeneity on geodetic data, and the strength of the lower crust in the Salton Trough region, southern California, *J. Geophys. Res.*, *110*, B09401, doi:10.1029/2004JB003548.

Fialko, Y. (2006), Interseismic strain accumulation and the earthquake potential on the southern San Andreas fault system, *Nature*, *441*(7096), 968–971.

Freed, A. M., and J. Lin (2001), Delayed triggering of the 1999 Hector Mine earthquake by viscoelastic stress transfer, *Nature*, *411*(6834), 180–183.

Fricker, H. A., A. Borsa, B. Minster, C. Carabajal, K. Quinn, and B. Bills (2005), Assessment of ICESat performance at the Salar de Uyuni, Bolivia, *Geophys. Res. Lett.*, *32*, L21S06, doi:10.1029/2005GL023423.

Fumal, T. E., M. J. Rymer, and G. G. Seitz (2002), Timing of large earthquakes since AD 800 on the Mission Creek strand of the San Andreas fault zone at Thousand Palms Oasis, near Palm Springs, California, *Bull. Seismol. Soc Am.*, *92*(7), 2841–2860.

Grollimund, B., and M. D. Zoback (2000), Post glacial lithospheric flexure and induced stresses and pore pressure changes in the northern North Sea, *Tectonophysics*, *327*(1–2), 61–81.

Gurrola, L. D., and T. K. Rockwell (1996), Timing and slip for prehistoric earthquakes on the Superstition Mountain Fault, Imperial Valley, southern California, *J. Geophys. Res.*, *101*(B3), 5977–5985.

Hampel, A., and R. Hetzel (2006), Response of normal faults to glacial-interglacial fluctuations of ice and water masses on Earth's surface, *J. Geophys. Res.*, *111*, B11408, doi:10.1029/2005JB004121.

Heki, K. (2001), Seasonal modulation of interseismic strain buildup in northeastern Japan driven by snow leads, *Science*, *293*(5527), 89–92.

Heki, K. (2003), Snow load and seasonal variation of earthquake occurrence in Japan, *Earth Planet. Sci. Lett.*, *207*(1–4), 159–164.

Hetland, E. A., and B. H. Hager (2006), Interseismic strain accumulation: Spin-up, cycle invariance, and irregular rupture sequences, *Geochem. Geophys. Geosyst.*, *7*, Q05004, doi:10.1029/2005GC001087.

Hetzel, R., and A. Hampel (2005), Slip rate variations on normal faults during glacial-interglacial changes in surface loads, *Nature*, *435*(7038), 81–84.

Hudnut, K. W., Y. Bock, J. E. Galetzka, F. H. Webb, and W. H. Young (2002), The Southern California Integrated GPS Network (SCIGN), in *Seismotectonics in Convergent Plate Boundary*, edited by Y. Fujinawa and A. Yoshida, pp. 167–189, Terra Sci., Tokyo.

Kaufmann, G., and F. Amelung (2000), Reservoir-induced deformation and continental rheology in vicinity of Lake Mead, Nevada, *J. Geophys. Res.*, *105*(B7), 16,341–16,358.

King, G. C. P., and M. Cocco (2001), Fault interaction by elastic stress changes: New clues from earthquake sequences, *Adv. Geophys.*, *44*, 1–38.

King, G. C. P., R. S. Stein, and J. Lin (1994), Static stress changes and the triggering of earthquakes, *Bull. Seismol. Soc Am.*, *84*(3), 935–953.

Larson, K. M. (1990), Precision, accuracy, and tectonics from the Global Positioning System, Ph.D. thesis, 269 pp., Univ. of Calif., San Diego, La Jolla, Calif.

Love, A. E. H. (1929), The stress produced in a semi-infinite solid by pressure on part of the boundary, *Proc. Roy. Soc. Lond. A*, *228*, 377–420.

Matmon, A., D. P. Schwartz, R. Finkel, S. Clemmens, and T. Hanks (2005), Dating offset fans along the Mojave section of the San Andreas fault using cosmogenic Al-26 and Be-10, *Geol. Soc. Am. Bull.*, *117*(5–6), 795–807.

Nelson, S. T., M. J. Wood, A. L. Mayo, D. G. Tingey, and D. Eggett (2005), Shoreline Tufa and Tufaglomerate from Pleistocene Lake Bonneville, Utah, USA: Stable isotopic and mineralogical records of lake conditions, processes, and climate, *J. Quat. Sci.*, *20*(1), 3–19.

Oglesby, L. C. (2005), *The Salton Sea: Geology, History, Potential Problems, Politics, and Possible Futures of an Unnatural Desert Salt Lake*, *Memoirs of the Southern California Academy of Sciences*, vol. 10, 240 pp., S. Calif. Acad. of Sci., Los Angeles, Calif.

Oskin, M., L. Perg, D. Blumentritt, S. Mukhopadhyay, and A. Iriondo (2007), Slip rate of the Calico fault: Implications for geologic versus geodetic rate discrepancy in the Eastern California Shear Zone, *J. Geophys. Res.*, *112*, B03402, doi:10.1029/2006JB004451.

Reasenberg, P. A., and R. W. Simpson (1992), Response of regional seismicity to the static stress change produced by the Loma-Prieta Earthquake, *Science*, *255*(5052), 1687–1690.

Roeloffs, E. A. (1988a), Fault stability changes induced beneath a reservoir with cyclic variations in water level, *J. Geophys. Res.*, *93*(B3), 2107–2124.

Roeloffs, E. A. (1988b), Hydrologic precursors to earthquakes—A review, *Pure Appl. Geophys.*, *126*(2–4), 177–209.

Shifflett, H., M. G. Gray, R. Grannell, and B. L. Ingram (2002), New evidence on the slip rate, renewal time, and late Holocene surface displacement, southernmost San Andreas fault, Mecca Hills, California, *Bull. Seismol. Soc Am.*, *92*(7), 2861–2877.

Sieh, K. E., and P. L. Williams (1990), Behavior of the southernmost San Andreas fault during the past 300 years, *J. Geophys. Res.*, *95*(B5), 6629–6645.

Simpson, D. W., W. S. Leith, and C. H. Scholz (1988), Two types of reservoir-induced seismicity, *Bull. Seismol. Soc Am.*, *78*(6), 2025–2040.

Smith, B., and D. Sandwell (2003), Coulomb stress accumulation along the San Andreas fault system, *J. Geophys. Res.*, *108*(B6), 2296, doi:10.1029/2002JB002136.

Smith, B., and D. Sandwell (2004), A three-dimensional semianalytic viscoelastic model for time-dependent analyses of the earthquake cycle, *J. Geophys. Res.*, *109*, B12401, doi:10.1029/2004JB003185.

Thomas, A. P., and T. K. Rockwell (1996), A 300- to 550-year history of slip on the Imperial fault near the US-Mexico border: Missing slip at the Imperial fault bottleneck, *J. Geophys. Res.*, *101*(B3), 5987–5997.

Turcotte, D. L., and G. Schubert (2002), *Geodynamics*, 456 pp., Cambridge Univ. Press, New York.

Waters, M. R. (1983), Late Holocene Lacustrine chronology and archaeology of ancient Lake Cahuilla, California, *Quat. Res.*, *19*(3), 373–387.

B. Bills, Y. Bock, K. Luttrell, and D. Sandwell, Scripps Institution of Oceanography, La Jolla, CA 92093-0225, USA. (kluttrell@ucsd.edu)

B. Smith-Konter, Planetary Science and Life Detection Section, Jet Propulsion Laboratory, California Institute of Technology, Pasadena, CA 91109, USA.